

Limitations in Wavelet Analysis of Non-Stationary Atmospheric Gravity Wave Signatures in Temperature Profiles

Robert Reichert^{1,2}, Natalie Kaifler², and Bernd Kaifler²

¹Meteorological Institute Munich, Ludwig-Maximilians-University, Munich, Germany

²Deutsches Zentrum für Luft- und Raumfahrt, Institut für Physik der Atmosphäre, Oberpfaffenhofen, Germany

Correspondence: Robert Reichert (robert.reichert@physik.uni-muenchen.de)

Abstract. Continuous Wavelet Transform (CWT) is a commonly used mathematical tool when it comes to the time-frequency (or distance-wavenumber) analysis of non-stationary signals and is used in a variety of research areas. In this work we use the CWT to investigate signatures of atmospheric internal gravity waves (GW) as observed in vertical temperature profiles obtained for instance by lidar. The focus is laid on the determination of vertical wavelengths of dominant GWs. According to linear GW theory these wavelengths are a function of horizontal wind speed and hence, vertical wind shear causes shifts in the evolution of the vertical wavelength. The resulting signal fulfills the criteria of a chirp. Using complex Morlet wavelets, we apply CWT to test mountain wave signals modeling wind shears of up to $5 \text{ m s}^{-1} \text{ km}^{-1}$ and investigate the capabilities and limitations. We find that the sensitivity of the CWT decreases for large chirp rates, i.e. strong wind shear. For a 4th order Morlet wavelet, edge effects become dominant at a vertical wind shear of $3.4 \text{ m s}^{-1} \text{ km}^{-1}$. For higher-order wavelets, edge effects dominate at even smaller values. In addition, we investigate the effect of GW amplitudes growing exponentially with altitude on the determination of vertical wavelengths. It becomes evident that, in case of conservative amplitude growth, spectral leakage leads to artificially enhanced spectral power at lower altitudes. Therefore, we recommend to normalize the GW signal before the wavelet analysis and the determination of vertical wavelengths. Finally, the cascading of receiver channels which is typical for middle atmosphere lidar measurements results in an exponential saw-tooth-like pattern of measurement uncertainties as function of altitude. With the help of Monte Carlo simulations we compute a wavelet noise spectrum and determine significance levels, which enables the reliable determination of vertical wavelengths. Finally, the insights obtained from the analysis of artificial chirps are used to analyse and interpret real GW measurements from the Compact Rayleigh Autonomous Lidar in April 2018 at Río Grande, Argentina. The comparison of results of commonly used and our suggested wavelet analysis demonstrates improvements in the accuracy of determined wavelengths. For future analyses, we suggest the usage of a 4th order Morlet wavelet, the normalization of GW amplitudes before wavelet analysis, and the significance level computation based on measurement uncertainties.

1 Introduction

The wavelet transform is a powerful mathematical tool to study non-stationary signals in time series and images. In contrast to the Fourier analysis, which decomposes a signal into a sum of sine and cosine functions, the wavelet analysis decomposes

25 the signal into a finite number of localized wavelets (Daubechies, 1990). It thus localizes signatures of interest in both time and frequency, making it a valuable tool for analyzing non-stationary signals. The wavelet transform has been used in a wide range of applications such as denoising (e.g. Pan et al., 1999; Alfaouri and Daqrouq, 2008; Tian et al., 2023), compression (e.g. Boix and Canto, 2010), feature extraction (e.g. Bruce et al., 2002; Seena and Yomas, 2014) and classification (e.g. Lambrou et al., 1998; Too et al., 2019) and is often applied to geophysical data (e.g. Torrence and Compo, 1998; Kaifler et al., 2017; 30 Bauer et al., 2020; Jin and Duan, 2021; Reichert et al., 2021). While the discrete wavelet transform is computationally cheap, it cannot capture the continuous time evolution of a signal. The continuous wavelet transform (CWT) provides a continuous representation of the signal in the time-frequency (or distance-wavenumber) domain, which makes it useful for analyzing signals that show time-dependent frequency variations.

One example of such non-stationary signals are perturbations in air density and temperature caused by atmospheric internal 35 gravity waves (GW). These are localized and intermittent phenomena (Fritts and Alexander, 2003) that are generated due to e.g. flow over orography (e.g. Queney, 1948; Dörnbrack et al., 1999; Kaifler et al., 2015), propagating Rossby wave trains (e.g. Dörnbrack et al., 2022), and regions of strong wind shear (e.g. Fritts, 1982). Their spectral properties such as frequency and wavenumber are functions of atmospheric background conditions like stratification and wind shear which are rarely zero in the real atmosphere and hence, transient conditions most of the time result in non-stationary GW signals. The vertical wavelength 40 of stationary mountain waves (MW) excited by flow over orography is approximately given as $\lambda_z = 2\pi \frac{u}{N}$ where u is the horizontal wind in the direction of wave propagation and N is the thermal stability (Nappo, 2013). Since u and N are in most cases not constant in the real atmosphere, the vertical wavelength changes with altitude and time. In this work we investigate whether the CWT is a suitable tool to analyse the change in wavelength due to wind shears of different strengths.

We focus on three major aspects of the CWT. First, one parameter that must be chosen is the non-dimensional frequency or 45 order m_0 of the wavelet. In case of the Morlet wavelet the order can be interpreted as the number of oscillations within the localization window. It determines the width of the wavelet in the time- and frequency-domain. A high order results in better frequency and worse time resolution, while the opposite is true for a low order. However, the order must not become arbitrary small as the admissibility condition must be fulfilled, i.e. the integral over the wavelet must be zero. In literature, there is no consensus on the optimal order of the Morlet wavelet. Many studies use an order of 6, as given in the widely cited work by 50 Torrence and Compo (1998). Other studies dealing with GW analysis use orders of 2, 4, 5 or 6.2 (see Table 1). However, the choice of the order plays an important role in the determination of vertical wavelengths as these can change rapidly depending on vertical wind shear.

Secondly, according to linear GW theory, not only can vertical wavelengths change rapidly, but the amplitudes of GWs also vary with altitude. Generally, amplitudes increase exponentially with altitude enforced by conservation of energy and decreasing 55 air density. However, when thermal or dynamical instability is reached, wave dissipation occurs, causing GW amplitudes to decrease above the breaking altitude. This variation in GW amplitude may lead to an undesirable shift in the localization of the wavelet during the computation of the CWT. To our knowledge, only few studies have normalized their GW signals before the wavelet analysis in order to prevent amplitude growth-induced errors (Wright et al., 2017; Vadas et al., 2018; Strelnikova et al., 2020; Gisinger et al., 2022).

Publication	Latitude	Height range	T' separation method	Significance	COI	order m_0	Uncertainties	Range of λ_z
(Chane-Ming et al., 2000)	21°S	30-60 km	Temporal mean subtraction and vertical Butterworth filtering	$T' > 1$ K	-	5.336	up to 0.86 %	1-10 km
(Werner et al., 2007)	69°N	30-60 km	Polynomial fit	50 % of T' maximum	-	6.2	-	3-8.5 km
(Rauthe et al., 2008)	54°N	1-105 km	Nightly mean subtraction	-	yes	5	1.5-2.5 K, never exceed 10 K	6-48 km
(Ehard et al., 2016)	68°N	30-65 km	Sliding cubic spline	-	yes	6	-	7-12 km
(Baumgarten et al., 2017)	54°N	30-70 km	Daily mean subtraction and Butterworth filtering	-	yes	-	-	3-20 km
(Reichert et al., 2021)	54°S	15-95 km	subtraction of long-period subseasonal oscillations	Spectral power >50 % of T uncertainty	yes	4	0.3-10 K	4-30 km
(Wing et al., 2021)	tropical	15-95 km	Nightly mean subtraction and Butterworth filtering	-	yes	-	0.1 K, never exceed 10 %	4-7 km
(Gisinger et al., 2022)	54°S	15-80 km	Butterworth filtering	-	yes	2	-	2-15 km

Table 1. Overview of publications dealing with vertical wavelength determination in lidar temperature soundings using the CWT. Every study has used the complex Morlet wavelet in their analysis.

60 Table 1 lists publications that determine vertical wavelengths of GWs based on wavelet analysis. While the discussion on background and perturbation separation is a common one and has been summarized, for instance, by Ehard et al. (2015), we seek to establish guidelines on best practices for the determination of vertical wavelengths. We note that all listed works address measurement uncertainties and significance levels in the wavelet power spectrum (WPS) differently, if at all. Also, the cone of influence (COI) that indicates the region where edge effects may influence the WPS is not dealt with or not even mentioned in

65 some papers. Therefore, as the third and last aspect of our work, we address the propagation of measurement uncertainties into the WPS, the computation of significance levels and hence the reliability of determined vertical wavelengths.

Ultimately, it is important to determine the vertical wavelength of GWs correctly since this parameter provides valuable information on the dynamics of the mean-flow. A shrinking vertical wavelength, for instance, may be indicative of a reduction in horizontal wind speed and, in extreme cases when the wavelength approaches zero, may point to a critical level, i.e. a level

70 where the intrinsic phase speed of a GW becomes equal to the horizontal wind speed and GW dissipation occurs. In addition, the vertical wavelength is a crucial quantity in raytracing (Marks and Eckermann, 1995; Geldenhuys et al., 2021) and is used in the computation of GW momentum fluxes (e.g. Ern et al., 2022). Moreover, knowledge about the vertical wavelength is necessary to derive temperature amplitudes and momentum fluxes in the mesosphere lower thermosphere from OH-airglow observations (Fritts et al., 2014).

Our considerations culminate in the following three questions:

1. What is the optimal choice for the order of the Morlet wavelet given a considerable vertical wind shear that gives rise to shifts in vertical wavelength of GWs?
2. Assuming a conservative growth rate of GW amplitudes with altitude, what is the benefit of normalizing GW amplitudes before applying the wavelet analysis?
3. How do measurement uncertainties affect the results of wavelet analysis and, in particular, which parts of the WPS can be trusted to representing reliable power estimates?

This publication is structured as follows. In Section 2 we first give a brief repetition on the mathematical foundation of the CWT and define four linear chirps as test signals. After that we investigate the research questions in Section 3 based on the defined test signals and, subsequently, we present a case study demonstrating the application of wavelet analysis to GW signatures observed by the CORAL lidar in Argentina. Section 4 discusses the results and Section 5 gives a summary, conclusions, and recommendations on how to determine vertical wavelengths of non-stationary GW signatures in the middle atmosphere in the form of short step-by-step instructions.

2 Methods

2.1 Continuous Wavelet Transform

In the following we will recall the building blocks of the CWT and introduce the commonly used terms. The interested reader is referred to Torrence and Compo (1998); Maraun and Kurths (2004); Ge (2008) for detailed information.

The core of the CWT is the mother wavelet that is in this work chosen to be the complex Morlet wavelet and given as

$$\psi_0(\eta) = \pi^{-1/4} e^{im_0\eta} e^{-\eta^2/2} \quad (1)$$

where η is the non-dimensional length and m_0 is the non-dimensional wavenumber. m_0 is also called order of the Morlet wavelet. Morlet wavelets are a class of wavelets that are commonly used in geophysics (e.g. Grinsted et al., 2004; Wong et al., 2012; Kaifler et al., 2017; Llamedo et al., 2019; Wu et al., 2021; Reichert et al., 2021; Geldenhuys et al., 2022). Daughter wavelets are scaled (s) and translated (ξ) versions of the mother wavelet such that

$$\psi(\xi, s) = c(s) \psi_0\left(\frac{z - \xi}{s}\right), \quad (2)$$

where z is altitude and $c(s)$ is a normalization factor. Three Morlet wavelets with orders of 4, 6, and 8 are illustrated in Figure 1. Normalization can be performed in two different ways: Either one requires a flat white noise spectrum or sines of the same amplitude having the same integrated power in the wavenumber domain. Torrence and Compo (1998) have defined $c(s) = \sqrt{\frac{\delta z}{s}}$ which results in a flat white noise spectrum but sines of same amplitude have less spectral power at larger scales. In order to allow for a fair comparison of peaks in the WPS we follow Maraun and Kurths (2004) and references therein and

105 define $c(s) = \sqrt{\delta z}$, where δz is the vertical sampling interval.

The CWT of a temperature signal $T(z)$ is given by the convolution with the set of daughter wavelets:

$$W(z, s) = c(s) \int_{z_i}^{z_f} T(z) \psi^*(z - \xi, s) d\xi \quad (3)$$

$$= c(s) \int_{-m_{max}}^{m_{max}} \hat{T}(m) \hat{\psi}^*(m, s) e^{imz} dm, \quad (4)$$

110 where z_i and z_f define the altitude range of the measurement, $(^*)$ indicates the complex conjugate, $(\hat{\cdot})$ indicates the Fourier transform, and $m_{max} = \frac{1}{2\delta z}$. Equation 4 makes use of the convolution theorem. As the Morlet wavelet is complex, also the wavelet transform is complex and the WPS is defined as $|W(z, s)|^2$.

The scales of the daughter wavelets are computed as

$$s_j = s_0 2^{j\delta j}, \quad j = 0, 1, \dots, J \quad (5)$$

$$J = \frac{1}{\delta j} \log_2 \left(\frac{N\delta z}{s_0} \right), \quad (6)$$

115 where s_0 is the smallest resolvable scale and set to $s_0 = 2\delta z$, $\delta j = \frac{1}{16}$, and J determines the largest scale which depends on the altitude range of the measurement.

In case of non-periodic signals, the computed spectral power at the edges of the WPS, i.e. where $z - z_i < \sqrt{2}s$ or $z_f - z < \sqrt{2}s$, where z_i and z_f are starting and ending altitudes respectively, is not reliable and might be overestimated. The factor $\sqrt{2}s$ is called e -folding time (in our context e -folding length) and ensures that spectral power from edge discontinuities drops by a factor of e^{-2} . This e -folding length region where the spectral power at the edges of the WPS is affected by discontinuities is commonly referred to as the cone of influence (COI). Larger orders result in a larger extend of the Morlet wavelet and hence to a more extended COI in the WPS. It is suggested to pad the profile with zeros up to the next power of two before applying the CWT. This results in an underestimation of spectral power at the edges and a speed up of the FFT algorithm.

The chosen scales are not necessarily identical to wavelengths. The conversion is given by

$$125 \quad \lambda = \frac{2\pi s}{m_0 + \sqrt{2 + m_0^2}}. \quad (7)$$

A scale of $s = 5$ km is equivalent to a wavelength of 3.9 km for an order of 4 and 7.6 km for an order of 8 (see Fig. 1). Werner et al. (2007) have chosen an order of 6.2 which ensures that scales and wavelengths are identical. In the next sections we define four linear chirps $LC_i(z)$ that serve as test signals with well-known wavelengths $\lambda_{input}(z)$, amplitudes $a(z)$, and noise levels $r(z)$. Subsequently, the CWT of $LC_i(z)$ are computed and the locations of the maxima in the WPS are used to determine the $\lambda_{output}(z)$ as function of altitude. The ratio of output to input wavelength is used as a metric to quantify how well the wavelet analysis has captured the chirp.

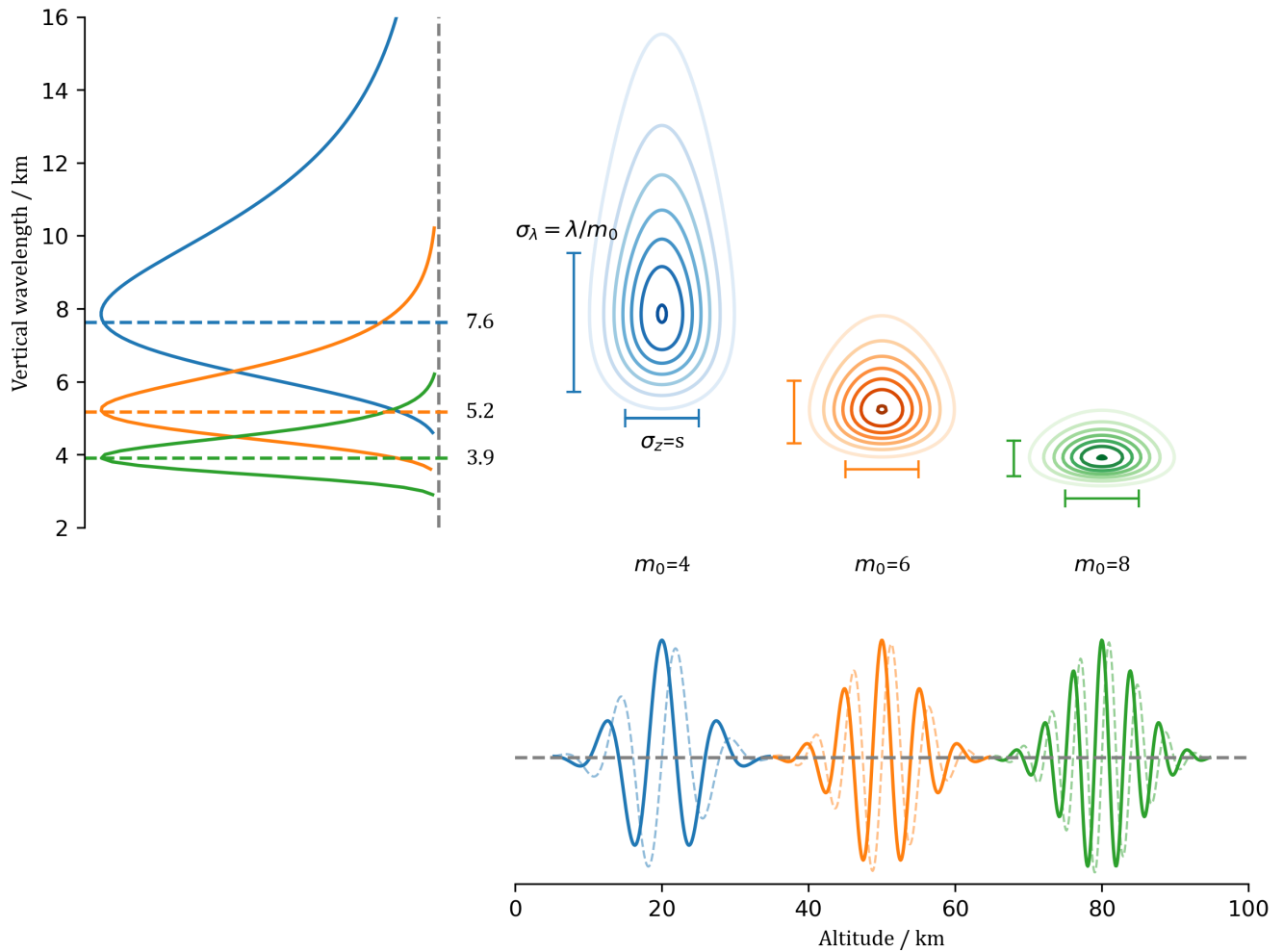


Figure 1. Illustration of three wavelets and their spectral representation with identical scale $s = 5$ km but different orders (blue: $m_0 = 4$, orange: $m_0 = 6$, green: $m_0 = 8$). Solid (dashed) lines show the real (imaginary) part of the Morlet wavelet. Contours show the representation of each wavelet in the $z - \lambda_z$ -space. Horizontal and vertical bars mark the standard deviation in z and λ_z respectively.

2.2 Definition of test signals

To assess the performance of the wavelet analysis we define four linear chirps according to

$$LC_i(z) = a_i(z) \sin \left(2\pi \int_0^z \frac{1}{\lambda_i(\tilde{z})} d\tilde{z} \right) + r_i(z) \quad (8)$$

135 where $a_i(z)$ are amplitudes, $r_i(z)$ are random numbers from a Gaussian distribution with mean $\mu = 0$ and standard deviation σ_i , and the vertical wavelengths λ_i are given as

$$\lambda_i(z) = \frac{2\pi\partial_z u_i}{N} z + \lambda_0, \quad (9)$$

140 where $N = 0.02\text{s}^{-1}$, $\lambda_0 = 0.2\text{ km}$, and z ranges from 0 km to 100 km. The first two chirps, LC_1 and LC_2 , have constant amplitudes of $a_{1,2} = 1.0\text{ K}$, no additive white Gaussian noise $\sigma_{1,2} = 0.0\text{ K}$, and differ only by the chirp rates which are computed from wind shears of $\partial_z u_1 = 5\text{ m s}^{-1}\text{ km}^{-1}$ and $\partial_z u_2 = 2.5\text{ m s}^{-1}\text{ km}^{-1}$, which are typical values for a real atmosphere (Fig.2a, b). The latter two chirps, LC_3 and LC_4 , have a chirp rate according to a wind shear of $\partial_z u_{3,4} = 2.5\text{ m s}^{-1}\text{ km}^{-1}$, show a linear amplitude growth with growth rate $\gamma = 1.0\text{ K km}^{-1}$ according to $a_{3,4}(z) = 1.0\text{ K} + \gamma z\text{ K}$ but differ in their additive Gaussian white noise levels. While LC_3 has no additive noise, LC_4 shows a constant noise level a standard deviation of $\sigma_4 = 5\text{ K}$, and uncorrelated values every 100 m (Fig.2c, d). An overview of the chirp parameters is given in Table 2.

	a / K	$\partial_z u / \text{m s}^{-1}\text{ km}^{-1}$	σ / K
LC_1	1.0	5.0	0.0
LC_2	1.0	2.5	0.0
LC_3	$\gamma z + 1.0$	2.5	0.0
LC_4	$\gamma z + 1.0$	2.5	5.0

Table 2. Parameter of the four defined linear chirps.

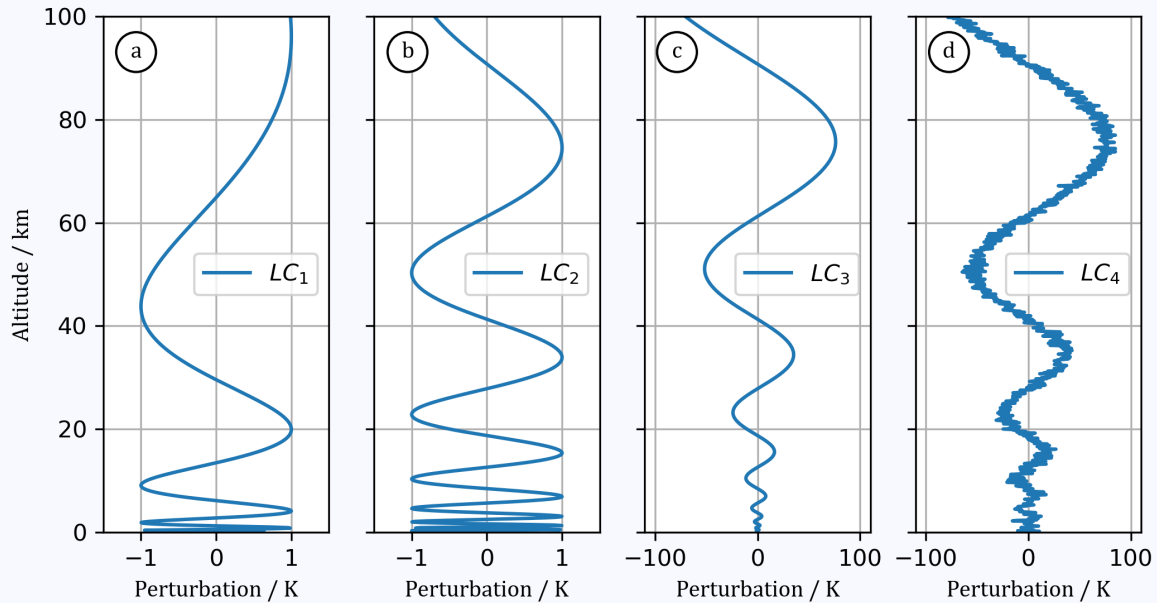


Figure 2. Four defined linear chirps with either constant (a,b) or linearly growing (c,d) amplitudes. Wavelengths derived from wind shears of $5 \text{ m s}^{-1} \text{ km}^{-1}$ (a) and $2.5 \text{ m s}^{-1} \text{ km}^{-1}$ (b,c,d) change linearly. The added Gaussian white noise is $\sigma = 0 \text{ K}$ (a,b,c) and $\sigma = 5 \text{ K}$ (d).

145 3 Results

3.1 What is the optimal choice for the order of the Morlet wavelet?

Figure 3 illustrates the WPS of LC_1 and LC_2 using wavelet orders of 4 and 6. We focus on the lowermost 50 km since vertical wavelengths increase further above and the WPS maximum lies completely in the COI there. When using a 6th order wavelet, we find that the WPS maximum of LC_2 is entirely within the COI (Fig. 3a). Comparing the evolution of input and output wavelengths, we find mostly good agreement but also one discontinuity at 35 km. This discontinuity disappears when using a 4th order wavelet (Fig. 3b), resulting in the WPS maximum being now outside the COI. We notice that output wavelengths are at all altitudes shorter than input wavelengths. When increasing the wind shear to $5 \text{ m s}^{-1} \text{ km}^{-1}$, the WPS maximum of LC_1 is located within the COI and again a discontinuity occurs (Fig. 3c).

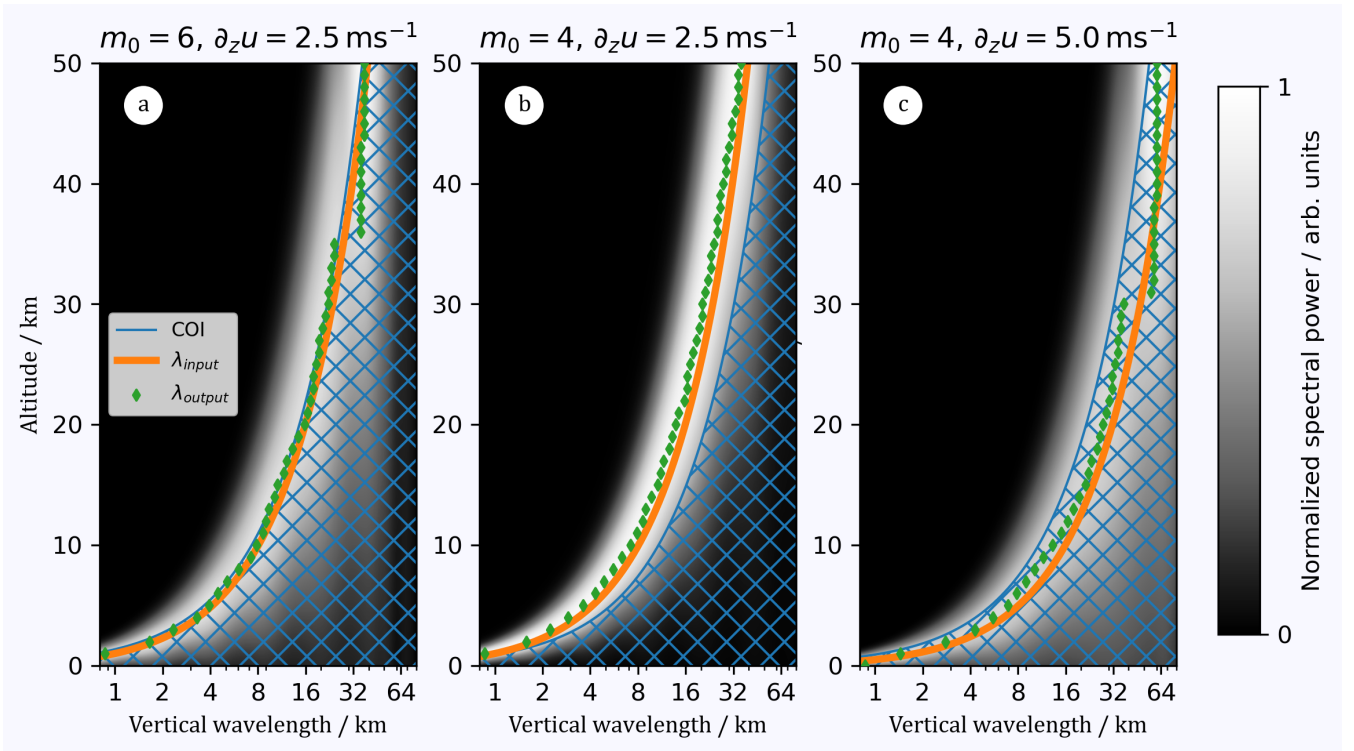


Figure 3. WPS of LC_2 using $m_0 = 6$ (a), $m_0 = 4$ (b), and WPS of LC_1 using $m_0 = 4$ (c). Orange lines mark the input wavelength as function of altitude and green diamonds mark the determined output wavelength, i.e. the maximum in the WPS at each z . The hatched blue regions mark the COI.

To quantify the level of agreement between input and output wavelength we compute their ratio as function of wind shear and wavelet order. For that we generate more linear chirps similar to LC_1 and LC_2 with constant amplitudes, no additive noise, and wavelengths computed from wind shears in the range $0.5 - 4.5 \text{ m s}^{-1} \text{ km}^{-1}$. We compute the WPS using wavelet orders of 4, 6, and 8 and determine the output wavelengths as the WPS maxima. Figure 4 illustrates the distributions of wavelength ratios derived from the lowermost 50 km of the simulated altitude range and Table 3 lists the corresponding median deviations as well as interquartile ranges (IQR). We find an average negative deviation from the input wavelength of $\approx -10\%$ for $m_0 = 4$, while the IQR stays below 10% for all considered wind shears. For wavelet orders of 6 and 8 we notice smaller median deviations from unity, while the IQR exceeds 10% starting at a wind shear of $3.0 \text{ m s}^{-1} \text{ km}^{-1}$ and $2.0 \text{ m s}^{-1} \text{ km}^{-1}$, respectively. The increase in IQR is most likely due to increasing edge effects such as mentioned discontinuities shown in Figure 3a,c. The e -folding line marking the COI can also be understood as a chirp rate that corresponds to a maximum wind shear up until edge effects are negligible. Assuming a constant $N = 0.02 \text{ s}^{-1}$ for the case $m_0 = 4$, the maximum wind shear that is reached until edge effects can be considered minor is $3.4 \text{ m s}^{-1} \text{ km}^{-1}$, for $m_0 = 6$ it is $2.3 \text{ m s}^{-1} \text{ km}^{-1}$, and for $m_0 = 8$ it is $1.8 \text{ m s}^{-1} \text{ km}^{-1}$. These values are in line with the broadening of the wavelength ratio distributions in Figure 4 and the notable increase in IQRs in Table 3.

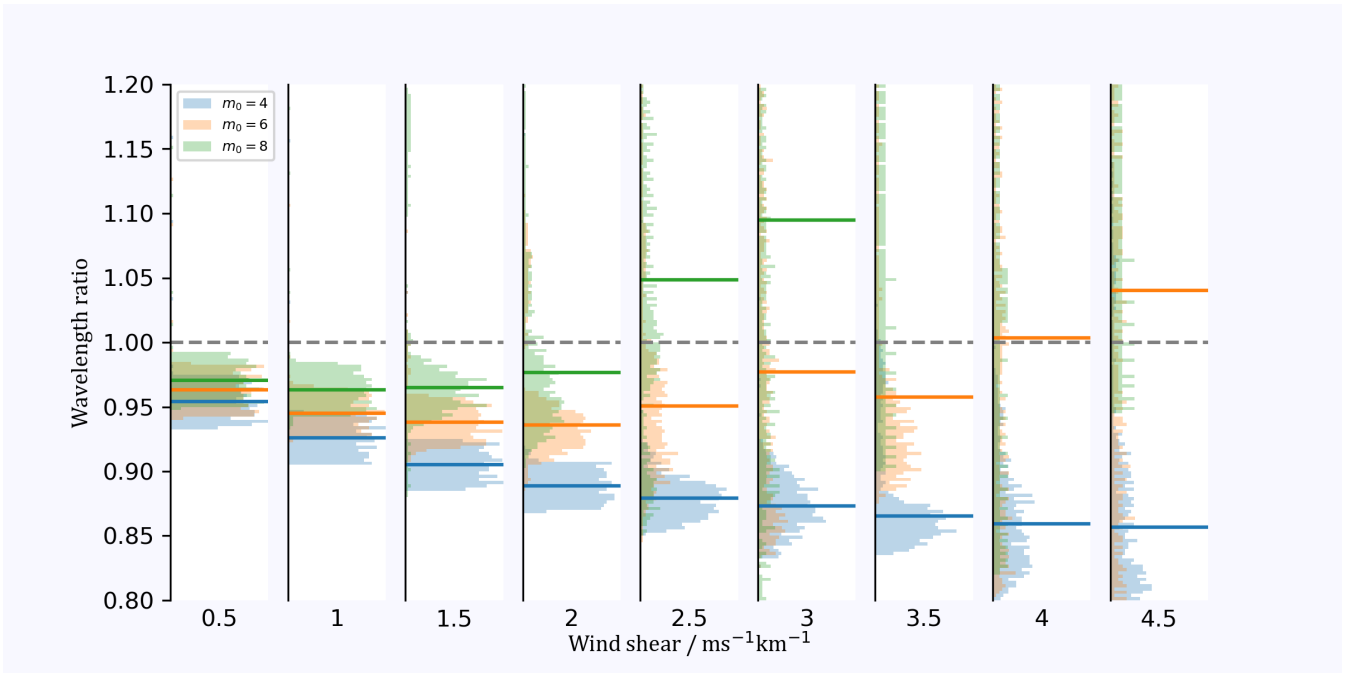


Figure 4. Normalized histograms of the wavelength ratio as function of wind shear and wavelet order (blue: $m_0 = 4$, orange: $m_0 = 6$, green: $m_0 = 8$). The determination of wavelengths is based on linear chirps with constant amplitude and no additive noise. Horizontal lines represent the median of the distribution. Note that for $m_0 = 8$ and wind shear $> 3.5 \text{ m s}^{-1} \text{ km}^{-1}$ the median lies outside the plot range. The grey dashed line marks a wavelength ratio of one. See Table 3 for details.

$\partial_z u / \text{m s}^{-1} \text{ km}^{-1}$	0.5	1.0	1.5	2.0	2.5	3.0	3.5	4.0	4.5
$m_0 = 4$	$-4.6^{+1.1}_{-1.1}$	$-7.4^{+1.0}_{-1.1}$	$-9.5^{+1.0}_{-1.0}$	$-11.1^{+1.0}_{-1.0}$	$-12.1^{+1.0}_{-1.1}$	$-12.7^{+1.7}_{-1.4}$	$-13.5^{+2.7}_{-1.2}$	$-14.1^{+3.0}_{-2.7}$	$-14.3^{+5.3}_{-4.3}$
$m_0 = 6$	$-3.7^{+1.1}_{-1.1}$	$-5.5^{+1.1}_{-1.0}$	$-6.2^{+1.1}_{-1.0}$	$-6.4^{+1.6}_{-1.3}$	$-4.9^{+4.3}_{-3.8}$	$-2.2^{+12.9}_{-8.9}$	$-4.2^{+26.0}_{-3.9}$	$0.4^{+15.1}_{-10.8}$	$4.0^{+23.1}_{-14.8}$
$m_0 = 8$	$-3.0^{+1.1}_{-1.1}$	$-3.7^{+1.0}_{-1.0}$	$-3.5^{+1.4}_{-1.4}$	$-2.3^{+8.3}_{-2.8}$	$4.8^{+12.7}_{-7.0}$	$9.6^{+24.4}_{-15.1}$	$80.0^{+>100}_{-59.8}$	$57.2^{+>100}_{-51.7}$	$89.0^{+>100}_{-62.9}$

Table 3. Median deviation from a wavelength ratio of unity and IQR in percent as function of wind shear and wavelet order. Green cells mark distributions with an IQR smaller than 10%.

3.2 What is the benefit of normalizing GW amplitudes before applying the wavelet analysis?

It is expected that GW amplitudes grow exponentially with altitude in the absence of dissipation due to conservation of energy since air density decreases with altitude. Do amplitudes growing with altitude affect the determination of vertical wavelengths in the wavelet analysis? To investigate potential effects, we consider the general solution to the Taylor-Goldstein equation for $u = 0 \text{ m s}^{-1}$ and without loss of generality at $x = t = 0$. Furthermore, for simplicity, we limit our analysis to the solution for

an upward propagating wave. See also equations 2.54-2.56 in Nappo (2013). The GW's temperature signature is given as

$$T(z) = T_0 e^{z/2H} e^{im_0 z/s}, \quad (10)$$

175 where T_0 is an arbitrary initial temperature and H is the density scale height that is in the middle atmosphere in the order of 6-8 km. The product of $T(z)$ with the complex conjugate daughter Morlet wavelet at $\xi = 0$ evaluates to

$$T(z)\psi^*(z, s) = T_0 e^{z/2H} e^{im_0 z/s} \cdot \pi^{-1/4} e^{-im_0 z/s} e^{-z^2/2s^2} \quad (11)$$

$$= T_0 \pi^{-1/4} e^{z/2H} e^{-z^2/2s^2}. \quad (12)$$

The position of the peak of this product is not in agreement with the peak of the Morlet wavelet's Gaussian window anymore
180 but is located at $z = \frac{s^2}{2H}$. It becomes clear that during the computation of the convolution (Eq. 4), due to the exponential growth of GW amplitudes, spectral power leaks from $z = z_0 + \frac{s^2}{2H}$ down to $z = z_0$. In other words, spectral amplitudes computed at (z, s) are dominated by wave amplitudes at $(z + \frac{s^2}{2H}, s)$. For example, assuming $H = 7$ km and a vertical wavelength of $\lambda_z = 2$ km, spectral leakage occurs over an altitude range of 0.5 km, while for a vertical wavelength of $\lambda_z = 10$ km spectral power leaks over an altitude range of 12 km. Figure 5 illustrates the consequences in case the wavelength is determined without
185 normalizing the amplitudes before the wavelet analysis. Output wavelengths identified as the maxima in the WPS of LC_3 deviate significantly from input wavelengths when amplitudes grow linearly (Fig. 5b). As mentioned above, due to spectral leakage, the WPS at low altitudes is strongly affected by large-scale large-amplitude signals at higher altitudes. Please note that increasing amplitudes affect the determination of wavelengths only in case the wavelength also changes with altitude.

We investigate whether a normalization of the signal before the wavelet analysis can mitigate the problem of spectral leakage.

190 We suggest the following: First, we compute the running root-mean-square (RMS) of the temperature perturbations over a boxcar window of length L . Ideally, L covers one vertical wavelength. A multiplication with a factor of $\sqrt{2}$ converts the running RMS of temperature perturbations into what can be considered GW amplitudes. Second, we fit a 4th degree polynomial to the derived GW amplitudes. Finally, we normalize the temperature perturbations by dividing them by the result of the polynomial fit. Following this procedure, the output wavelengths retrieved from the WPS are again in reasonable agreement with the input
195 wavelengths as demonstrated in Figure 5c.

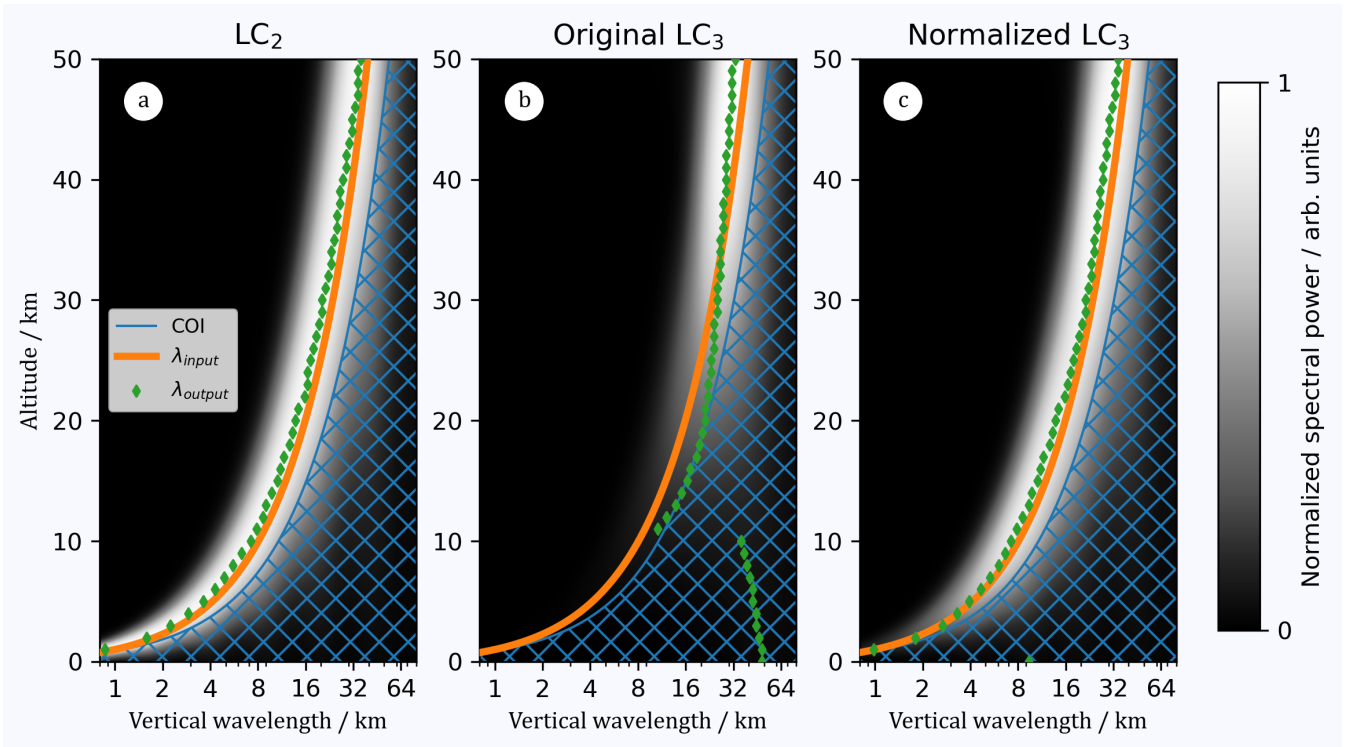


Figure 5. WPS of LC_2 (a), WPS of LC_3 (b), and WPS of LC_3 after amplitude normalization for $m_0 = 4$ (c). Orange lines mark the input wavelength and green diamonds mark determined output wavelengths, i.e. the maximum in the WPS at each z . The hatched blue regions mark the COI.

In order to further quantify the effect of growing amplitudes on the determination of vertical wavelengths, we multiply the linear chirps from Section 3.1 with linearly increasing amplitudes according to growth rates of 0.1 K km^{-1} , 1 K km^{-1} , and 10 K km^{-1} . The modified chirps are analysed with and without normalization using a 4th order wavelet. Distributions of wavelength ratios are illustrated in Figure 6 and median deviations from a wavelength ratio of unity as well as IQRs are given in Table 4.

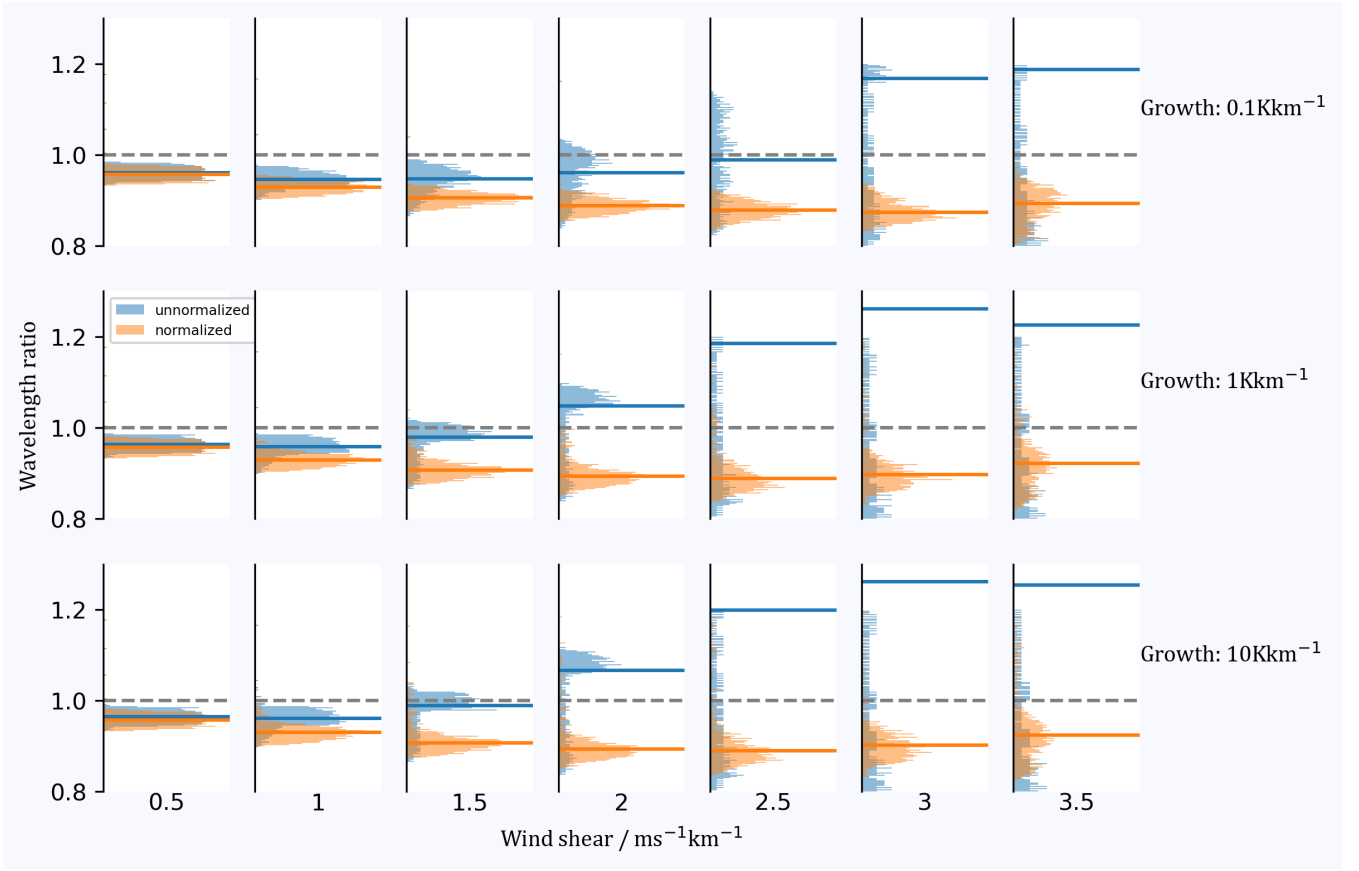


Figure 6. Normalized histograms of the wavelength ratio as function of wind shear and amplitude growth rate (blue: without normalization, orange: with normalization). The wavelet order is $m_0 = 4$. Horizontal lines represent the median of the distribution. The grey dashed lines mark a wavelength ratio of one. See Table 4 for details.

Growth rate	$\partial_z u / \text{ms}^{-1} \text{km}^{-1}$	0.5	1.0	1.5	2.0	2.5	3.0	3.5
0.1 K km ⁻¹	not normalized	$-3.9^{+1.1}_{-1.0}$	$-5.4^{+1.2}_{-1.1}$	$-5.3^{+1.5}_{-2.2}$	$-3.9^{+3.1}_{-4.5}$	$-1.1^{+6.5}_{-7.7}$	$16.9^{+22.4}_{-24.7}$	$18.7^{+>100}_{-28.1}$
	normalized	$-4.4^{+1.1}_{-1.0}$	$-7.2^{+1.0}_{-1.0}$	$-9.5^{+0.9}_{-1.0}$	$-11.2^{+1.1}_{-1.1}$	$-12.2^{+1.3}_{-1.3}$	$-12.6^{+1.7}_{-1.3}$	$-10.7^{+2.4}_{-2.7}$
1 K km ⁻¹	not normalized	$-3.6^{+1.0}_{-1.1}$	$-4.2^{+1.2}_{-1.2}$	$-2.1^{+1.5}_{-2.7}$	$4.8^{+2.3}_{-10.2}$	$18.5^{+19.3}_{-24.8}$	$26.4^{+>100}_{-33.8}$	$22.5^{+>100}_{-31.2}$
	normalized	$-4.3^{+1.0}_{-1.0}$	$-7.1^{+1.0}_{-1.1}$	$-9.3^{+1.3}_{-1.2}$	$-10.7^{+1.7}_{-1.4}$	$-11.2^{+2.6}_{-1.8}$	$-10.3^{+2.7}_{-1.9}$	$-7.9^{+3.8}_{-3.6}$
10 K km ⁻¹	not normalized	$-3.5^{+1.0}_{-1.1}$	$-3.9^{+1.3}_{-1.2}$	$-1.1^{+1.6}_{-3.4}$	$6.6^{+2.5}_{-11.8}$	$19.9^{+67.5}_{-26.2}$	$26.4^{+>100}_{-33.8}$	$25.5^{+>100}_{-34.1}$
	normalized	$-4.3^{+1.0}_{-1.0}$	$-7.0^{+1.1}_{-1.2}$	$-9.3^{+1.4}_{-1.2}$	$-10.6^{+1.8}_{-1.4}$	$-11.0^{+2.7}_{-1.9}$	$-9.8^{+2.9}_{-2.1}$	$-7.5^{+4.3}_{-3.5}$

Table 4. Median deviation from a wavelength ratio of one and IQR in percent as function of wind shear and growth rate. Green cells mark distributions with IQRs smaller than 10%.

We notice that for wind shears less than $1.5 \text{ m s}^{-1} \text{ km}^{-1}$ the wavelength ratio distributions deviate less from unity when no normalization is applied regardless of the amplitude growth rate. However, when wind shears exceed $2 \text{ m s}^{-1} \text{ km}^{-1}$, we find that the IQRs for not normalized chirps increase drastically while the normalization keeps the IQRs at a low level.

205 **3.3 How do measurement uncertainties affect the results of wavelet analysis and, in particular, which parts of the WPS can be trusted to representing reliable power estimates?**

Every measurement is subject to measurement uncertainties. To model a simple case, we assume a white noise spectrum. To distinguish a physically meaningful signal from noise, we need to know how the noise is reflected in the WPS. We propose the following approach: First, we generate 5,000 Gaussian white-noise profiles with a vertical resolution of 100 m, with $\mu = 0 \text{ K}$, and $\sigma = 5 \text{ K}$ and compute the WPS of each noise profile. From the set of 5,000 WPS we determine the 99th percentile of spectral power as function of z and λ_z . Any spectral power in the signal's WPS above this 99th percentile is considered to be significant on the 99 % level.

215 We now inspect the WPS of LC_4 (the linear chirp with growing amplitudes and added noise, Fig. 7a) and find a similar distribution of wavelengths as for LC_3 (the linear chirp with growing amplitudes without added noise, Fig. 5b). To mitigate the problem of spectral leakage due to growing wave amplitudes, we normalize LC_4 as described in Section 3.2 and obtain the results shown in Figure 7b. As evident from Figure 7b, the normalization results in an increase of spectral power of the linear chirp but also of noise notable below 10 km. In other words, where the signal-to-noise ratio is low (in this case below 2) the determination of vertical wavelengths is not reliable. It is crucial to compute significance levels to determine physically meaningful wavelengths.

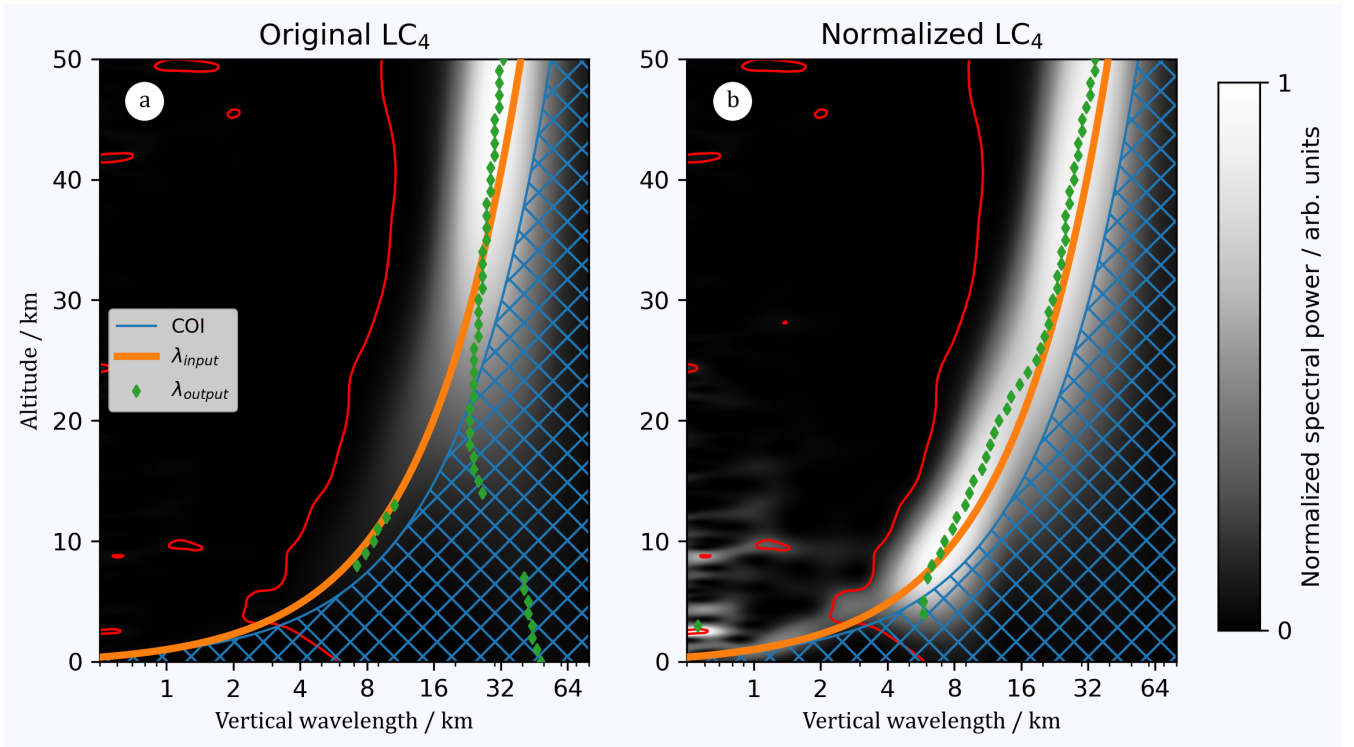


Figure 7. WPS of the original LC_4 (a) and of the normalized LC_4 (b). $m_0 = 4$ was used in the CWT. Red contours mark the 99% significance level. Orange lines mark the input wavelength and green diamonds determined output wavelengths, i.e. the maximum in the WPS at each z . The hatched blue regions mark the COI.

3.4 Application to Lidar Temperature Profiles

220 In the following we apply the wavelet analysis to a temperature profile obtained by the Compact Rayleigh Autonomous Li-
 225 230 dar (CORAL). CORAL is a mobile lidar system developed and built by the German Aerospace Center (DLR) and provides
 temperature measurements from approximately 15 km to 100 km altitude. For details see Kaifler and Kaifler (2021). In this
 work, we analyze a temperature profile obtained at Río Grande (53.7°S, 67.7°W), Argentina, on the night of 21 May 2018
 00UTC. The profile shown in Figure 8a is binned in the vertical to 100 m resolution with statistical independent values every
 900 m. We use this example to demonstrate the CWT analysis and substantiate the points raised in previous sections, as well as
 show the limitations of the CWT with respect to the wavelet analysis of non-stationary GW signals. The temperature profile in
 Figure 8a shows significant temperature variability which can be attributed to MWs. Río Grande is in the lee of the Southern
 Andes and is known to be a hotspot for GWs, in particular MWs (e.g. Hoffmann et al., 2013; Hindley et al., 2020; Rapp et al.,
 2021; Reichert et al., 2021). The temperature uncertainty peaks at 30 km and 45 km where receiving channels are switched,
 and at altitudes above 90 km. In an initial step, potential GW signals are separated from a thermal larger-scale background.
 This can be realised in multiple ways. We follow Ehard et al. (2015) and apply a 5th order high-pass Butterworth filter with a

cutoff wavelength of 20 km to the temperature profile in order to separate the temperature background from the GW-induced temperature perturbations. In addition, we compute the theoretically expected upper limit of vertical wavelengths using the Brunt Väisälä frequency determined from the derived temperature background and horizontal winds from ERA5 reanalysis and juxtapose the measured vertical wavelength using our best practice (Fig. 8d). Reanalysis data is spectrally truncated at wavenumber T21 in order to define a synoptic-scale background (e.g. Reichert et al., 2021).

After separating the background temperature profile (Fig. 8a) from GW-induced perturbations (Fig. 8b), we apply the polynomial fit as suggested in Section 3.2 in order to derive GW amplitudes. A maximum growth rate of 0.82 K km^{-1} is found at 36 km. The polynomial fit is used to normalize the perturbations before applying the wavelet analysis. Results show short vertical wavelengths and a minimum in GW amplitudes at altitudes of about 25 km. Above, vertical wavelengths become longer and amplitudes increase towards a maximum of 20 K at 55 km. Temperature perturbations are dominated by small scales above 80 km.

The ERA5 profiles of zonal and meridional wind show a rather steady increase of wind speeds between 20 km and 50 km. The vertical shear of horizontal wind exceeds $3.4 \text{ m s}^{-1} \text{ km}^{-1}$ between 32 km and 37 km. At this altitude, we find a discontinuity in the profile of measured vertical wavelengths. Computed and measured vertical wavelengths agree quite well below 35 km but differ by up to a factor of two above 35 km. This is our test case for the application of the CWT.

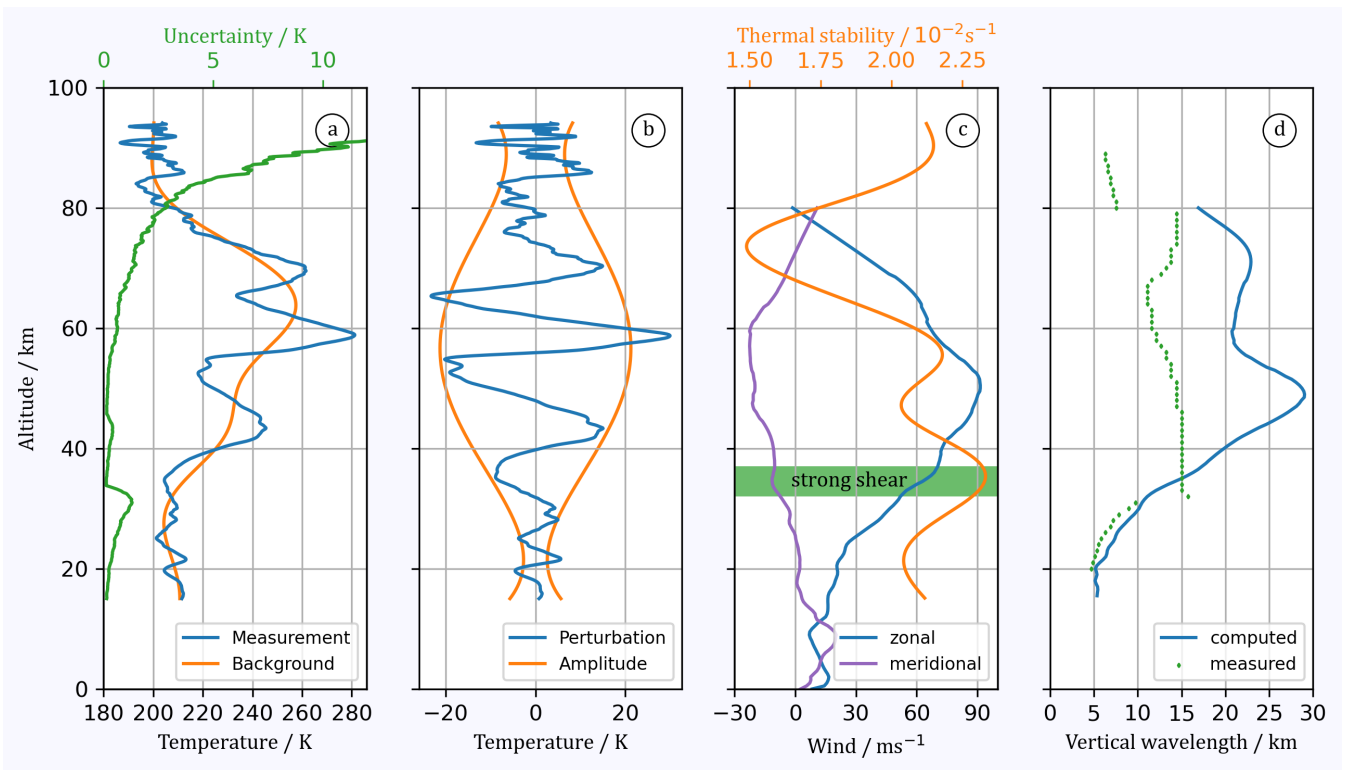


Figure 8. (a) Temperature profile obtained by CORAL on the night 21 May 2018 00UTC (blue), associated temperature uncertainties (green), and determined temperature background (orange). (b) Associated temperature perturbation (blue) and wave amplitude (orange). (c) Zonal (blue) and meridional (purple) wind speed from ERA5 and stratification (orange). The green region marks altitudes where the wind shear exceeds $3.4 \text{ m s}^{-1} \text{ km}^{-1}$. (d) Maximum vertical wavelength calculated from ERA5 wind and CORAL background temperature profiles (blue) and measured vertical wavelengths (green).

3.4.1 Analysis of measurement noise

Figure 9 shows the result of our noise analysis based on uncertainties in lidar retrieved temperatures. The procedure is similar to that described in Section 3.3. We generate 5,000 noise profiles with uncorrelated values every 100 m, a mean of $\mu = 0$ and a standard deviation corresponding to the temperature uncertainty at the respective altitude. Subsequently, we compute 5,000 WPS and determine the 99th percentile which is presented in Figure 9. The saw-tooth pattern in the profile of measurement uncertainties (Fig. 8a) is reflected in enhancements of spectral power at corresponding altitudes. If we look at the horizontal stripes with maximum spectral power, we note that these maxima become wider towards longer wavelengths. This is probably due to the fact that the wavelet's localization is weaker at longer wavelengths and noise from distant altitudes contributes to the WPS.

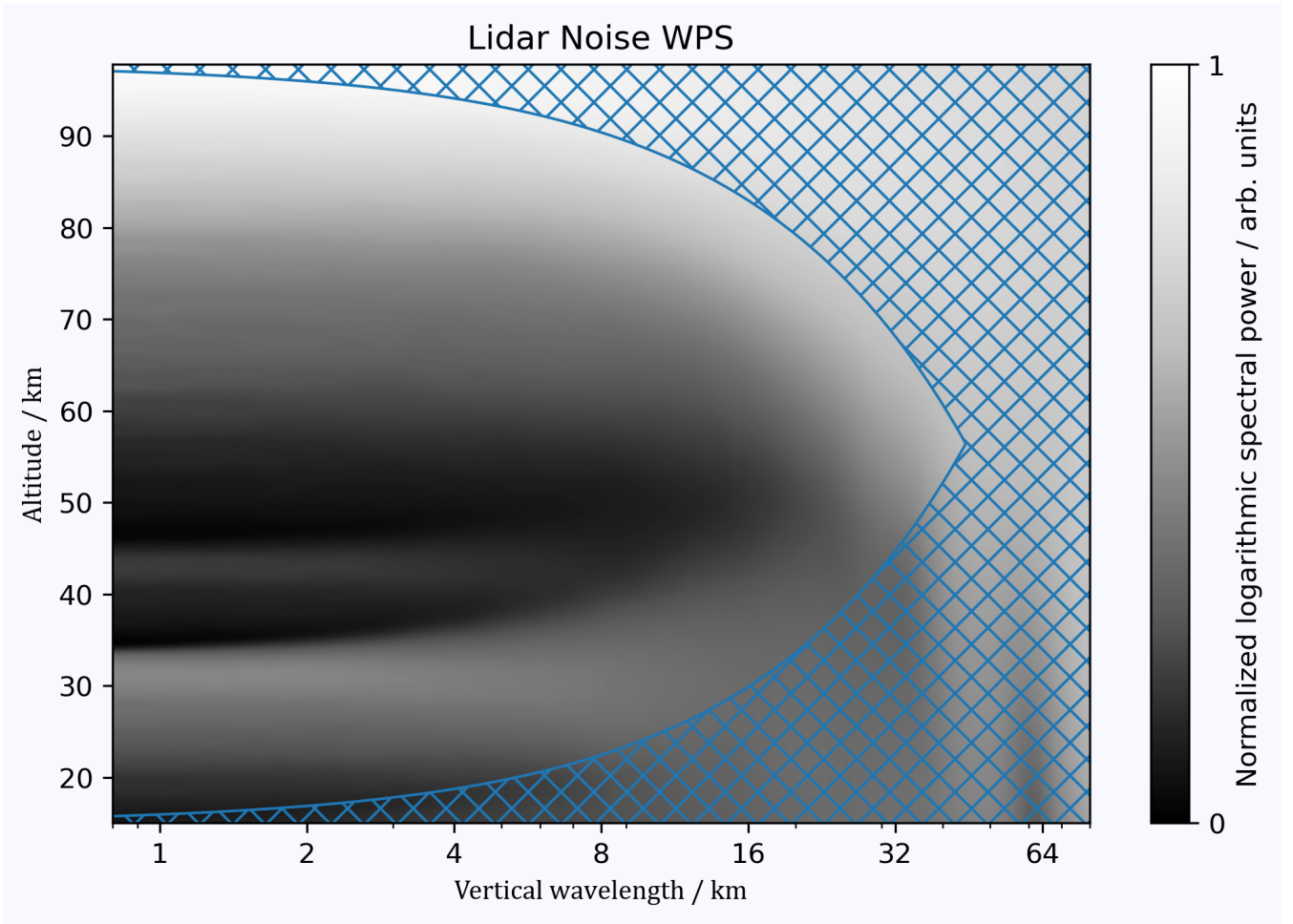


Figure 9. 99th percentile computed from 5,000 WPS of lidar measurement uncertainties. The hatched blue region marks the COI.

3.4.2 Wavelet analysis of GW-induced temperature perturbations

We now create a WPS in the conventional way in which the amplitudes of the temperature disturbance are not normalized, the order of the wavelet is set to $m_0 = 6$, and no significance levels are determined (Fig. 10a). Furthermore, we create a WPS based on our best-practice procedure where the amplitudes of the temperature perturbation are normalized, the order of the wavelet is set to $m_0 = 4$, and significance levels are calculated (Fig. 10b). In the conventional WPS we find only little variation in the vertical wavelength with values ranging from $\lambda_z = 12.7$ km to 16.4 km. Values decrease from the upper and lower edge of the profiles towards 65 km altitude. Considering the COI, λ_z is reliable between 35 km and 75 km altitude only. The conventional WPS shows no other interesting features. Let us now turn to the best-practice WPS (Fig. 10b). Similar to the conservative case, we find an extended altitude region from 30 km to 80 km with only little variation in the vertical wavelength with values of $\lambda_z = 11.1$ km to 15.0 km which are smaller than the values found in the conservative case. This agrees with the results from our

sensitivity study (Section 3.1). In contrast to the conventional case we are able to identify maxima in the WPS now at vertical wavelengths from $\lambda_z = 4.7$ km at 20 km altitude to $\lambda_z = 9.8$ km at 30 km altitude and vertical wavelengths in the order of 6 km to 7 km above 80 km altitude.

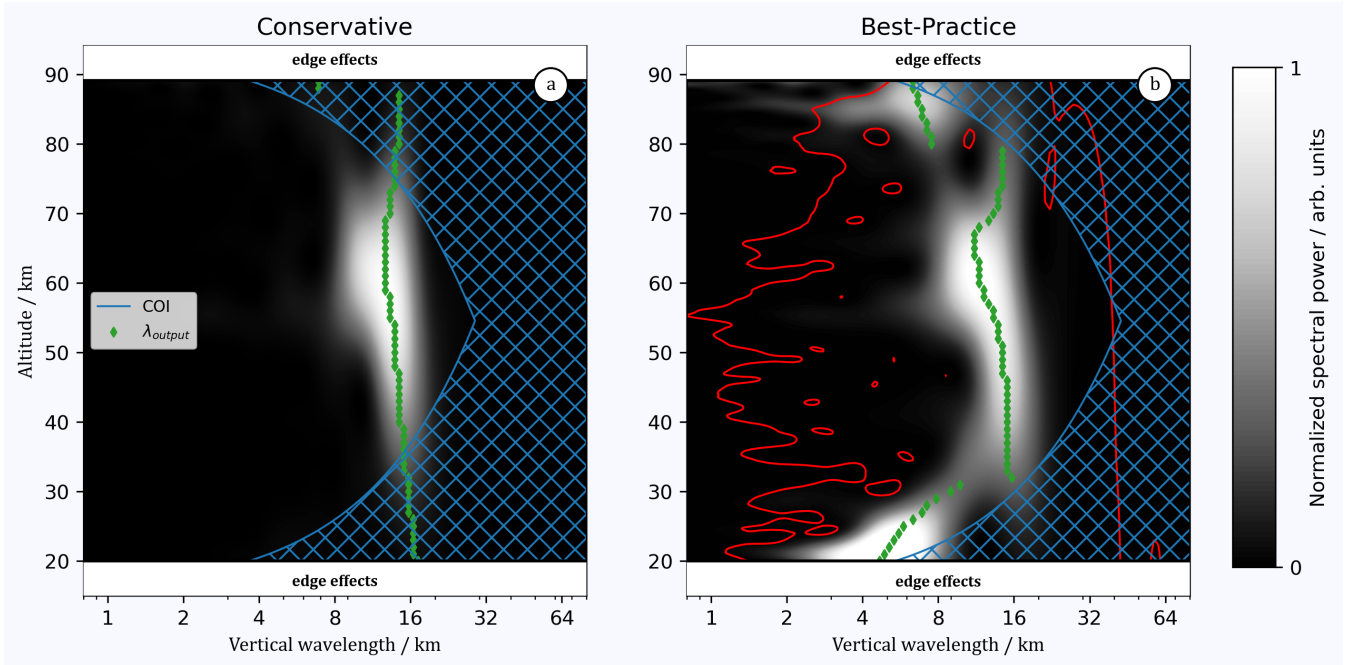


Figure 10. (a) WPS of measured temperature perturbations from 21 May 2018 00UTC for $m_0 = 6$. (b) Same as (a) but following best practices in the computation of the WPS. Green diamonds mark the derived vertical wavelengths, i.e. the maxima in the WPS at each z . The red line marks the 99 % significance level. The hatched blue regions mark the COI.

4 Discussion

270 We investigated the choice of wavelet order, amplitude normalization, and determination of significance levels using linear chirps. To a first approximation, i.e. for sufficiently short height regions, it can be assumed that the vertical wavelength of GWs changes linearly. The study of linear chirps using the CWT shows the limitations of the CWT, but also how these limitations can be extended if necessary and what consequences this has for the interpretation of the results.

In general, multiple GWs can overlap in space and time and one has to investigate not only the global maximum but also
 275 local maxima in the WPS to separate individual GWs. This was done, for instance, by Chane-Ming et al. (2000); Rauthe et al. (2008); Baumgarten et al. (2017); Reichert et al. (2021); Mori et al. (2021). However, in order to systematically investigate the limitations of wavelet analysis with respect to its ability to separate superimposed GWs, further analyses which are beyond the scope of this work, are necessary.

4.1 The choice of m_0

280 Linear GW theory shows that vertical wavelengths of GWs are a function of the horizontal wind speed. Therefore, vertical
wind shear causes shifts in the vertical wavelength of GWs. Our test cases suggest that the resolvable chirp rate is sensitive
to the order of the wavelet (Fig. 4). When the shear region is stronger localized than the wavelet itself, edge effects influence
the WPS and thus the determined wavelengths. We suggest to first inspect background wind and stability in order to make an
educated guess of the GW's wavelength shift. Depending on the expected chirp rate, we recommend to use the highest order
285 wavelet possible in the CWT computation since we find that the accuracy of the determined wavelengths decreases for lower
order wavelets. As an example, consider a MW signal modulated by a wind shear of $4.5 \text{ m s}^{-1} \text{ km}^{-1}$. The highest possible
wavelet order that should be used to study the signal is $m_0 = 4$, since the accuracy of the determination of the wavelength
decreases significantly when higher orders are used (see Table 3). However, if the wind shear is only $1.5 \text{ m s}^{-1} \text{ km}^{-1}$, a wavelet
order of $m_0 = 8$ should be used, since the accuracy of the determination of the wavelength is better for this order than for lower
290 orders. That in mind, it is very likely that the distribution of vertical wavelengths presented in Reichert et al. (2021) is biased
towards shorter wavelengths since they used a fourth order wavelet in their wavelet analysis. On the other hand, Reichert et al.
(2021) did not normalize GW signatures, which can have the opposite effect leading to overestimated vertical wavelengths
(Fig. 6).

Edge effects arising from weak wavelet localization become a problem in regions where strong wind shear is expected, such
295 as the mid-latitude wintertime lower stratosphere. For the example presented in Figure 8 we find wind shears exceeding
 $3.4 \text{ m s}^{-1} \text{ km}^{-1}$ in the lower stratosphere (Fig. 8c) and even values of up to $7 \text{ m s}^{-1} \text{ km}^{-1}$ are not rare in austral winter in
the Southern Andes region. As expected from reanalysis winds, it is the region of strongest shear where the dominant vertical
wavelength transitions quickly from $\lambda_z = 10 \text{ km}$ to $\lambda_z = 15 \text{ km}$ in the WPS (Fig. 10b). Following the traditional analysis, this
jump might be interpreted as a hint on two distinct and often termed "quasi-monochromatic" wave packets. However, with
300 our new best-practice approach there is evidence that the observed signature reflects a MW undergoing a rapid wavelength
shift. ERA5 temperature perturbation fields and co-located OH-airglow imagery (both not shown) provide more evidence that
the MW observed by CORAL propagates steeply within the lidar's field of view. On the other hand, the difference between
computed and measured vertical wavelength (Fig. 8d) could be an indication for an obliquely propagating MW. After all, this
work is of methodological nature and the geophysical interpretation of the results is not in our focus.

305 As shown in this work, the best choice of m_0 depends on the expected wavelength shift and therefore, background wind shear
and thermal stability should be investigated before applying wavelet analysis.

4.2 GW amplitude normalization

According to linear theory, GW amplitudes increase exponentially with altitude in the absence of dissipation. We demonstrated
in Section 2.1 that the exponential variation of GW amplitudes results in spectral leakage of wavelet power to altitudes with
310 smaller GW amplitudes and hence, growing GW amplitudes lead to inaccuracies in determined vertical wavelengths. To our
knowledge, no other work has yet investigated this effect even though it appears the effect is known in literature as for example

Gisinger et al. (2022) normalized GW signals when comparing lidar measurements and results from a numerical weather prediction model, and Vadas et al. (2018) scaled temperature perturbations with density. However, they did not investigate systematic differences between WPS of normalized and unnormalized GW signals. In this work, we normalized the GW signals by dividing them by a fourth degree polynomial obtained by a fit to the wave amplitudes. The order of the polynomial should be such that it has as little energy as possible at wavelengths in the spectral range of interest. We found that regardless of the growth rate it is better to not normalize GW signals as long as the wind shear remains weaker than about $1.5 \text{ m s}^{-1} \text{ km}^{-1}$ (Table 4). As the wind shear increases, normalization provides better results. In particular, the wavelength ratios are less scattered (see distributions in Fig. 6). At the same time, however, normalization leads to a systematic underestimation of the vertical wavelength, as already shown in the case of constant amplitudes (Table 3). Again, we suggest to inspect background wind profiles before applying wavelet analysis and normalize GW signals when wind shears larger than $1.5 \text{ m s}^{-1} \text{ km}^{-1}$ are expected.

Since the wind shear in the case study (Fig. 8c) easily exceeds the $1.5 \text{ m s}^{-1} \text{ km}^{-1}$, we normalized the temperature perturbations before applying the CWT. It is this additional step which allowed us to capture the evolution of the MW (see Fig. 10b), revealing an increase of vertical wavelength from $\lambda_z = 10 \text{ km}$ to $\lambda_z = 15 \text{ km}$ at approximately 32 km altitude.

4.3 Significance levels in wavelet power spectra

Chane-Ming et al. (2000); Werner et al. (2007); Reichert et al. (2021) used temperature amplitudes to determine whether signals of interest are reliable. By doing so they made the implicit assumption of a flat noise spectrum. This may be approximately true for certain spectral regions, but generally this assumption cannot be made for real measurement data. For example, using wavelet analysis to investigate the noise in lidar data, we were able to show that the spectral amplitudes increase toward long vertical wavelengths, revealing the characteristics of red noise (Fig. 9). Therefore, even if the noise level is low at a specific altitude, a large scale signal could be potentially not significant at this very same altitude due to higher noise levels at distant altitudes. We argue that it is crucial to compute significance levels as described in Section 3.3 in order to reliably determine wavelengths. In our case study all maxima in the WPS are significant (Fig. 10).

5 Summary and Conclusion

We studied the determination of vertical wavelengths based on wavelet analysis using first artificial test signals and later lidar temperature measurements. We discussed the treatment of measurement uncertainties, the impact of GW amplitudes increasing with altitude, and the influence of chirps that arise due to the vertical shear of horizontal wind. Following tests with artificially created data, we presented a recipe which aims to minimize the influence of edge effects in wavelet analysis. For the analysis of lidar data, we suggest to first inspect atmospheric background variables such as horizontal wind speed and thermal stability and then, depending on the particular atmospheric conditions, choose the wavelet order which is most suitable for analyzing the data. For measurements taken at a mid-latitude site like Río Grande (54° S) in winter we set $m_0 = 4$. This choice has the advantage that for one the admissibility condition is still met and second, chirps due to wind shears of up to $\partial_z u = 4.5 \text{ m s}^{-1} \text{ km}^{-1}$

can be resolved. In addition, the e -folding length is smaller, resulting in weaker edge effects. Second, prior to the wavelet analysis, GW amplitudes usually should be normalized in order to prevent spectral leakage. In this work, a 4th degree polynomial fit was found to be a suitable normalization method. Third, the noise characteristic of the instrument is used to compute a noise-WPS which in turn is used to determine significance levels.

In the following, we give step-by-step instructions on how to analyze lidar data for GWs.

350 1. **Separation of background and perturbation**

Apply a 5th order Butterworth filter in the vertical. In a first substep, the cutoff is set to the maximum wavelength that can be expected from theoretical considerations, i.e. for mid-frequency MWs $\lambda_z \approx 2\pi \frac{u}{N}$. This cutoff is usually too large at first and is set in a second substep to the maximum wavelength that results from the *wavelength determination*. The Butterworth filter and other approaches are extensively discussed in Ehard et al. (2015).

355 2. **Amplitude Normalization**

Compute the running RMS of the temperature perturbation over a window size that is equal to the cutoff wavelength of the Butterworth filter. Fit a polynomial to the running RMS and use the result to normalize the perturbations. The polynomial fit should capture only large scales and the degree of the polynomial should be chosen such that the spectral power in the wavelength range containing GW signals remains approximately unaffected.

360 3. **Wavelength determination**

Compute the WPS of the normalized temperature perturbation profile. Create a profile of vertical wavelength by identifying maxima in the WPS at each altitude.

4. **Noise WPS computation**

365 Generate 5,000 Gaussian noise profiles with a standard deviation given by the measurement uncertainty as function of altitude. Compute the WPS of these profiles and determine the percentile of the WPS that is associated with the desired significance level.

5. **Assessment of significance levels**

370 Consider only vertical wavelengths in regions outside the COI and where the desired significance level is reached. Disregard the lower- and uppermost ~ 5 km in altitude because of edge effects from the Butterworth filtering as well as the *amplitude normalization*.

The presented limitations of wavelet analysis and work-arounds can be easily applied to temperature or wind profiles obtained, for instance, by other lidars and also by radars, radiosondes, and satellites. In essence, when choosing the wavelet transform for the investigation of GW signals in vertical profiles, one first must come up with an educated guess on expected wavelength shifts and amplitude growth. We found that the evolution of these two quantities determines in large parts the feasibility of the wavelet analysis.

Code and data availability. CORAL and ERA5 data are publicly available as netCDF and sav files at <https://doi.org/10.5281/zenodo.11119614>. IDL and Python routines are accessible via the same link.

Author contributions. RR developed the method, carried out all data analysis, and wrote the manuscript. NK and BK provided the CORAL data and revised the manuscript.

380 *Competing interests.* The authors declare that they have no conflict of interest.

Acknowledgements.

References

- Alfaouri, M. and Daqrouq, K.: ECG signal denoising by wavelet transform thresholding, *American Journal of applied sciences*, 5, 276–281, 2008.
- 385 Bauer, K., Norden, B., Ivanova, A., Stiller, M., and Krawczyk, C. M.: Wavelet transform-based seismic facies classification and modelling: application to a geothermal target horizon in the NE German Basin, *Geophysical Prospecting*, 68, 466–482, 2020.
- Baumgarten, K., Gerding, M., and Lübken, F.-J.: Seasonal variation of gravity wave parameters using different filter methods with daylight lidar measurements at midlatitudes, *Journal of Geophysical Research: Atmospheres*, 122, 2683–2695, 2017.
- Boix, M. and Canto, B.: Wavelet Transform application to the compression of images, *Mathematical and computer modelling*, 52, 1265–1270, 2010.
- 390 Bruce, L. M., Koger, C. H., and Li, J.: Dimensionality reduction of hyperspectral data using discrete wavelet transform feature extraction, *IEEE Transactions on geoscience and remote sensing*, 40, 2331–2338, 2002.
- Chane-Ming, F., Molinaro, F., Leveau, J., Keckhut, P., and Hauchecorne, A.: Analysis of gravity waves in the tropical middle atmosphere over La Reunion Island (21 S, 55 E) with lidar using wavelet techniques, in: *Annales Geophysicae*, vol. 18, pp. 485–498, 2000.
- 395 Daubechies, I.: The wavelet transform, time-frequency localization and signal analysis, *IEEE transactions on information theory*, 36, 961–1005, 1990.
- Dörnbrack, A., Leutbecher, M., Kivi, R., and Kyrö, E.: Mountain-wave-induced record low stratospheric temperatures above northern Scandinavia, *Tellus A: Dynamic Meteorology and Oceanography*, 51, 951–963, 1999.
- Dörnbrack, A., Eckermann, S. D., Williams, B. P., and Haggerty, J.: Stratospheric Gravity Waves Excited by a Propagating Rossby Wave Train—A DEEPWAVE Case Study, *Journal of the Atmospheric Sciences*, 79, 567–591, 2022.
- 400 Ehard, B., Kaifler, B., Kaifler, N., and Rapp, M.: Evaluation of methods for gravity wave extraction from middle-atmospheric lidar temperature measurements, *Atmospheric Measurement Techniques*, 8, 4645–4655, 2015.
- Ehard, B., Achtert, P., Dörnbrack, A., Gisinger, S., Gumbel, J., Khaplanov, M., Rapp, M., and Wagner, J.: Combination of lidar and model data for studying deep gravity wave propagation, *Monthly Weather Review*, 144, 77–98, 2016.
- 405 Ern, M., Preusse, P., and Riese, M.: Intermittency of gravity wave potential energies and absolute momentum fluxes derived from infrared limb sounding satellite observations, *Atmospheric Chemistry and Physics*, 22, 15 093–15 133, 2022.
- Fritts, D. C.: Shear excitation of atmospheric gravity waves, *Journal of Atmospheric Sciences*, 39, 1936–1952, 1982.
- Fritts, D. C. and Alexander, M. J.: Gravity wave dynamics and effects in the middle atmosphere, *Reviews of geophysics*, 41, 2003.
- Fritts, D. C., Pautet, P.-D., Bossert, K., Taylor, M. J., Williams, B. P., Iimura, H., Yuan, T., Mitchell, N. J., and Stober, G.: Quantifying gravity wave momentum fluxes with Mesosphere Temperature Mappers and correlative instrumentation, *Journal of Geophysical Research: Atmospheres*, 119, 13–583, 2014.
- 410 Ge, Z.: Significance tests for the wavelet cross spectrum and wavelet linear coherence, in: *Annales Geophysicae*, vol. 26, pp. 3819–3829, 2008.
- Geldenhuis, M., Preusse, P., Krisch, I., Zülicke, C., Ungermann, J., Ern, M., Friedl-Vallon, F., and Riese, M.: Orographically induced spontaneous imbalance within the jet causing a large-scale gravity wave event, *Atmospheric Chemistry and Physics*, 21, 10 393–10 412, 2021.

- Geldenhuis, M., Kaifler, B., Preusse, P., Ungermann, J., Alexander, P., Krasauskas, L., Rhode, S., Woiwode, W., Ern, M., Rapp, M., et al.: Observations of gravity wave refraction and its causes and consequences, *Journal of Geophysical Research: Atmospheres*, p. e2022JD036830, 2022.
- 420 Gisinger, S., Polichtchouk, I., Dörnbrack, A., Reichert, R., Kaifler, B., Kaifler, N., Rapp, M., and Sandu, I.: Gravity-Wave-Driven Seasonal Variability of Temperature Differences Between ECMWF IFS and Rayleigh Lidar Measurements in the Lee of the Southern Andes, *Journal of Geophysical Research: Atmospheres*, 127, e2021JD036270, 2022.
- Grinsted, A., Moore, J. C., and Jevrejeva, S.: Application of the cross wavelet transform and wavelet coherence to geophysical time series, *Nonlinear processes in geophysics*, 11, 561–566, 2004.
- 425 Hindley, N., Wright, C., Hoffmann, L., Moffat-Griffin, T., and Mitchell, N.: An 18-year climatology of directional stratospheric gravity wave momentum flux from 3-D satellite observations, *Geophysical research letters*, 47, e2020GL089557, 2020.
- Hoffmann, L., Xue, X., and Alexander, M.: A global view of stratospheric gravity wave hotspots located with Atmospheric Infrared Sounder observations, *Journal of Geophysical Research: Atmospheres*, 118, 416–434, 2013.
- Jin, Y. and Duan, Y.: 2d wavelet decomposition and fk migration for identifying fractured rock areas using ground penetrating radar, *Remote Sensing*, 13, 2280, 2021.
- 430 Kaifler, B. and Kaifler, N.: A Compact Rayleigh Autonomous Lidar (CORAL) for the middle atmosphere, *Atmospheric Measurement Techniques*, 14, 1715–1732, 2021.
- Kaifler, B., Kaifler, N., Ehard, B., Dörnbrack, A., Rapp, M., and Fritts, D. C.: Influences of source conditions on mountain wave penetration into the stratosphere and mesosphere, *Geophysical Research Letters*, 42, 9488–9494, 2015.
- 435 Kaifler, N., Kaifler, B., Ehard, B., Gisinger, S., Dörnbrack, A., Rapp, M., Kivi, R., Kozlovsky, A., Lester, M., and Liley, B.: Observational indications of downward-propagating gravity waves in middle atmosphere lidar data, *Journal of Atmospheric and Solar-Terrestrial Physics*, 162, 16–27, 2017.
- Lambrou, T., Kudumakis, P., Speller, R., Sandler, M., and Linney, A.: Classification of audio signals using statistical features on time and wavelet transform domains, in: *Proceedings of the 1998 IEEE International Conference on Acoustics, Speech and Signal Processing, ICASSP'98 (Cat. No. 98CH36181)*, vol. 6, pp. 3621–3624, IEEE, 1998.
- 440 Llamedo, P., Salvador, J., de la Torre, A., Quiroga, J., Alexander, P., Hierro, R., Schmidt, T., Pazmino, A., and Quel, E.: 11 years of Rayleigh lidar observations of gravity wave activity above the southern tip of South America, *Journal of Geophysical Research: Atmospheres*, 124, 451–467, 2019.
- Maraun, D. and Kurths, J.: Cross wavelet analysis: significance testing and pitfalls, *Nonlinear Processes in Geophysics*, 11, 505–514, 2004.
- 445 Marks, C. J. and Eckermann, S. D.: A three-dimensional nonhydrostatic ray-tracing model for gravity waves: Formulation and preliminary results for the middle atmosphere, *Journal of Atmospheric Sciences*, 52, 1959–1984, 1995.
- Mori, R., Imamura, T., Ando, H., Häusler, B., Pätzold, M., and Tellmann, S.: Gravity wave packets in the venusian atmosphere observed by radio occultation experiments: Comparison with saturation theory, *Journal of Geophysical Research: Planets*, 126, e2021JE006912, 2021.
- Nappo, C. J.: *An introduction to atmospheric gravity waves*, Academic press, 2013.
- 450 Pan, Q., Zhang, L., Dai, G., and Zhang, H.: Two denoising methods by wavelet transform, *IEEE transactions on signal processing*, 47, 3401–3406, 1999.
- Queney, P.: The problem of air flow over mountains: A summary of theoretical studies, *Bulletin of the American Meteorological Society*, 29, 16–26, 1948.

- Rapp, M., Kaifler, B., Dörnbrack, A., Gisinger, S., Mixa, T., Reichert, R., Kaifler, N., Knobloch, S., Eckert, R., Wildmann, N., et al.:
455 SOUTHTRAC-GW: An airborne field campaign to explore gravity wave dynamics at the world's strongest hotspot, *Bulletin of the American Meteorological Society*, 102, E871–E893, 2021.
- Rauthe, M., Gerding, M., and Lübken, F.-J.: Seasonal changes in gravity wave activity measured by lidars at mid-latitudes, *Atmospheric Chemistry and Physics*, 8, 6775–6787, 2008.
- Reichert, R., Kaifler, B., Kaifler, N., Dörnbrack, A., Rapp, M., and Hormaechea, J. L.: High-Cadence Lidar Observations of Middle Atmospheric Temperature and Gravity Waves at the Southern Andes Hot Spot, *Journal of Geophysical Research: Atmospheres*, 126,
460 e2021JD034 683, 2021.
- Seena, V. and Yomas, J.: A review on feature extraction and denoising of ECG signal using wavelet transform, in: 2014 2nd international conference on devices, circuits and systems (ICDCS), pp. 1–6, IEEE, 2014.
- Strelnikova, I., Baumgarten, G., and Lübken, F.-J.: Advanced hodograph-based analysis technique to derive gravity-wave parameters from
465 lidar observations, *Atmospheric Measurement Techniques*, 13, 479–499, 2020.
- Tian, C., Zheng, M., Zuo, W., Zhang, B., Zhang, Y., and Zhang, D.: Multi-stage image denoising with the wavelet transform, *Pattern Recognition*, 134, 109 050, 2023.
- Too, J., Abdullah, A. R., and Saad, N. M.: Classification of hand movements based on discrete wavelet transform and enhanced feature extraction, *International Journal of Advanced Computer Science and Applications*, 10, 2019.
- 470 Torrence, C. and Compo, G. P.: A practical guide to wavelet analysis, *Bulletin of the American Meteorological society*, 79, 61–78, 1998.
- Vadas, S. L., Zhao, J., Chu, X., and Becker, E.: The excitation of secondary gravity waves from local body forces: Theory and observation, *Journal of Geophysical Research: Atmospheres*, 123, 9296–9325, 2018.
- Werner, R., Stebel, K., Hansen, G., Blum, U., Hoppe, U.-P., Gausa, M., and Fricke, K.-H.: Application of wavelet transformation to determine wavelengths and phase velocities of gravity waves observed by lidar measurements, *Journal of Atmospheric and Solar-Terrestrial Physics*,
475 69, 2249–2256, 2007.
- Wing, R., Martic, M., Triplett, C., Hauchecorne, A., Porteneuve, J., Keckhut, P., Courcoux, Y., Yung, L., Retailleau, P., and Cocuron, D.: Gravity Wave Breaking Associated with Mesospheric Inversion Layers as Measured by the Ship-Borne BEM Monge Lidar and ICON-MIGHTI, *Atmosphere*, 12, 1386, 2021.
- Wong, S. H., Santoro, A. E., Nidziko, N. J., Hench, J. L., and Boehm, A. B.: Coupled physical, chemical, and microbiological measurements
480 suggest a connection between internal waves and surf zone water quality in the Southern California Bight, *Continental Shelf Research*, 34, 64–78, 2012.
- Wright, C. J., Hindley, N. P., Hoffmann, L., Alexander, M. J., and Mitchell, N. J.: Exploring gravity wave characteristics in 3-D using a novel S-transform technique: AIRS/Aqua measurements over the Southern Andes and Drake Passage, *Atmospheric Chemistry and Physics*, 17, 8553–8575, 2017.
- 485 Wu, S., Hu, Z., Wang, Z., Cao, S., Yang, Y., Qu, X., and Zhao, W.: Spatiotemporal variations in extreme precipitation on the middle and lower reaches of the Yangtze River Basin (1970–2018), *Quaternary International*, 592, 80–96, 2021.